




Passivity-Based PI Control for Receiver Side of Dynamic Wireless Charging System in Electric Vehicles

Jia Liu , Zhitao Liu , *Member, IEEE*, and Hongye Su , *Senior Member, IEEE*

Abstract—The dynamic wireless charging for electric vehicles (EVs) is considered an efficient and practical choice to extend the driving range and reduce battery pack size. However, the coupling coefficient between transmitter coils and receiver coil varies rapidly on a large scale during the EVs moving, so it deteriorates the charging performance of dynamic wireless power transfer in EVs, such as the discontinuous charging for the lithium-ion batteries in EVs. Moreover, the charging power and efficiency of the system can also be affected. To solve these issues, a dc–dc converter is added to cascade on the receiver side to improve the output power and efficiency of the system. Furthermore, the passivity-based proportional-integral control is designed for the dc–dc on the receiver side of dynamic wireless charging system to improve the performance against the rapidly changing coupling coefficient. Finally, compared with the conventional proportional-integral-derivative controller, simulation and experimental results are given to show the performance and robustness of dynamic wireless charging system by the proposed method.

Index Terms—Coupling coefficient, dynamic wireless charging, electric vehicles (EVs), passivity-based control (PBC), receiver side.

I. INTRODUCTION

WITH some good advantages, wireless power transfer (WPT) has been rapidly developed in recent several decades. Based on the magnetic coupling technique, it has been taken as an ideal charging method for electrical equipment, such as cell phones, smart home electrical appliances, pure electric vehicles (EVs), and plug-in hybrid electric vehicles (PHEVs) [1]–[5].

Manuscript received December 16, 2019; revised May 9, 2020, July 23, 2020, and November 9, 2020; accepted December 23, 2020. Date of publication January 14, 2021; date of current version September 29, 2021. This work was supported in part by the National Key R&D Program of China under Grant 2018YFA0703800, in part by the Science Fund for Creative Research Group of the National Natural Science Foundation of China under Grant 61621002, in part by the National Natural Science Foundation of China under Grant NSFC:61873233, in part by Zhejiang Key R&D Program under Grant 2021C01198, and in part by Ningbo Science and Technology Innovation 2025 Major Project under Grant 2019B10116. (*Corresponding author: Zhitao Liu.*)

The authors are with the State Key Laboratory of Industrial Control Technology, Institute of Cyber-Systems and Control, Zhejiang University, Hangzhou 310027, China (e-mail: liujia1019@zju.edu.cn; ztliu@zju.edu.cn; hysu@ipc.zju.edu.cn).

Color versions of one or more figures in this article are available at <https://doi.org/10.1109/TIE.2021.3050350>.

Digital Object Identifier 10.1109/TIE.2021.3050350

WPT was first used to power an EV by M. Hutin and M. Le-Blanc in 1894 [6], and it has been forgotten for around one hundred years, as a result of the drawback of power electronic technology and semiconductor. In the later 1970s, some scholars put increasing attention to wireless charging due to the energy crisis [1]–[3], [7], [8]. In 2007, Tesla’s experiment was verified by Prof. Soljagic’s group from MIT, and the WPT system designed by them was demonstrated to transfer 60 W with around 40% efficiency using strongly coupled magnetic resonance [9]. Wireless charging to EVs includes static wireless power transfer (SWPT) and dynamic wireless power transfer (DWPT). Furthermore, DWPT is regarded as a practical, economical, and environmental approach to deal with the range anxiety [3], [7]. By utilizing the dynamic wireless charging technique, EVs can pick up energy in-motion from the transmitter coils. The driving range can be considerably extended and, thus, the battery packs and the initial cost can be greatly reduced [4], [7].

There are two kinds of primary magnetic coupler structures in DWPT. The first one is the long track coupler, and a continuous charging power can be achieved when the receiver coil is moving over the transmitter track [10], [11]. However, the receiver coil is much smaller than the long track, resulting in a weak coupling condition. To solve the low efficiency and electromagnetic interference (EMI) caused by poor coupling coefficient, the segmental coupler structure is proposed in [12], and the transmitter coils are embedded separately along the lane. However, the coupling coefficient changes quickly on a large scale when a receiver coil is moving over the transmitter coils. Moreover, the misalignment is unavoidable during the dynamic charging process. The obstacles for DWPT are mainly about reducing charging power and the discontinuity of the lithium-ion battery charging process due to the widely changing coupling coefficient [7], [12], [13].

Some prior works have focused on the design of the compensation topology and magnetic coil to enhance the tolerance of the variable coupling coefficient in EVs moving. There are four basic compensation topologies named series-parallel (SP), series-series (SS), parallel-series (PS), and parallel-parallel (PP) [4]. Compared with other topologies, the double-sided inductor–capacitor–capacitor (LCC) topology proposed in [12], [14] shows a more robust characteristic against the variations of coupling coefficient and load conditions and, thus, a stable resonant condition could be achieved to reduce the control difficulty in DWPT scheme [14], [15]. Meanwhile, the double-sided

LCC network converts a voltage source on the primary side to a current source on the secondary side, which is suitable for EVs charging [16].

The magnetic coil structure is another crucial aspect of the DWPT system, and the commonly used magnetic structures for EVs charging are circular coil and rectangular coil. The circular pad is studied in [17], and the double-D (DD) couplers are studied and optimized in [18], while the double-D quadrature (DDQ) coils are designed in [19]. Compared with the segmental coupler, overlapped DD coil arrays are introduced to generate a relatively stable magnetic between the ground side coils and the moving coil [20], [21]. However, the coil arrays will increase the cost and the complexity of the DWPT system. Thus, some advanced control schemes are considered a practical and economical technology to solve these issues of the DWPT system.

The existing control schemes for DWPT can be classified into three categories: the transmitter-side control, the dual-side control, and the receiver-side control. A transmitter-side regulation methodology through current flow from the input source was proposed in [22], which is independent of the load conditions. In [23], a phase-shifting controller was presented using the output current or voltage in the primary side, without any direct measurement on the receiver side. However, each transmitter panel should be equipped with a controller, resulting in an intricate control design. A dual-side power control in [16] is proposed to increase the system efficiency with large coupling factor variations. However, the dual-side power control is regulated by phase shifting, the zero-voltage switch condition is destroyed, and it increases switching loss of insulated gate bipolar transistors (IGBTs). Meanwhile, dual-side control may suffer from the delay problems in communication, and therefore, it is not suitable for the DWPT system [4]. With lower implementation costs and avoiding communication delays, the receiver-side control strategy is a more appropriate choice for the DWPT system [7], [12]. An optimal equivalent load resistor tracking method was proposed through a dc–dc converter cascaded on the secondary side and, thus, high overall system efficiency can be achieved [24]. With a dc–dc converter on the secondary side, the real-time coupling coefficient estimation and the maximum efficiency control are provided to improve the transmitting efficiency of DWPT system [25]. Moreover, the dc–dc converter is designed to improve the wireless transfer power by adjusting the equivalent load. Apart from that, the control objectives to track the maximum efficiency and power improvement are different. During the short period of exiting one transmitter coil and entering another, transfer power regulation is more important than transmitting efficiency for EVs charging. Thus, the power transfer regulation is the first concern of our article.

In the DWPT system, the coupling coefficient changes rapidly on a large scale. The widely varying coupling coefficient will increase the difficulty of control design and deteriorates the performance of the system. Without fast regulation ability, conventional control methods cannot realize tracking control in case of the rapidly changing coupling coefficient, resulting in the fluctuation of the output voltage and current in DWPT. Therefore, the designed controller should have a rapid ability to regulate the dynamic system with fast varying parameters.

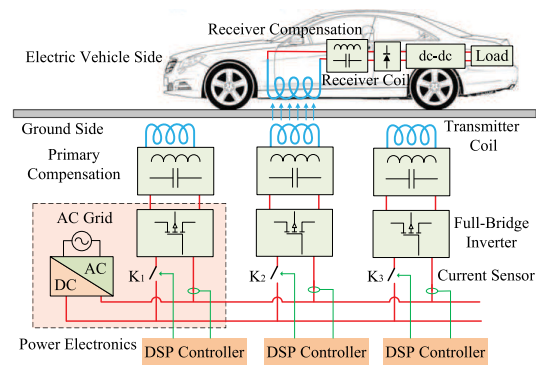


Fig. 1. DWPT system.

The proportional-integral-derivative (PID) controller is widely applied to buck dc–dc converters [26]. In [27], an adaptive backstepping control with the neural network was proposed to deal with the adjustment problem of a dc–dc buck converter. The major issue is that the computation of the duty ratio requires the estimation information of system parameters dynamically. It is not a suitable choice for practical applications. A second-order sliding-mode control (SMC) was proposed for the regulation of output voltage to track the reference value [28]. However, the shortcoming is that the chattering phenomena cause extremely high switching frequency, which is undesirable in industrial electronics schemes. Among these nonlinear control theories, passivity-based control (PBC) has attracted considerable attention. PBC was first proposed by Prof. Romeo Ortega, and so far, it has been applied in many different fields, such as mechanical, electrical, and electromechanical applications [29]–[34]. Moreover, passivity-based proportional-integral control (PIPBC) has more advantages, such as transient performance and robustness to unknown parameters [31], [35], [36]. Combined with PBC, PI is wrapped around a passive output. It is easy to guarantee the stability for the PI parameters gains [36].

In our article, by the above analysis of the dynamic charging for the lithium-ion batteries in EVs, a buck dc–dc converter is added to cascade on the receiver side in the DWPT system, and PIPBC is used to improve the performance and the robustness with the varying coupling coefficient. Furthermore, the simulation and experiment results are given to show the effectiveness and excellent performance of the proposed method.

The remaining of this article is organized as follows. In Section II, the structure and the magnetic coil of DWPT are analyzed, and the approach of receiver side power transfer regulation can be obtained. Section III shows the design of PIPBC. Simulation and experimental results are presented in Section IV and Section V, which are given to demonstrate the good performance of DWPT under PIPBC scheme. Finally, Section VI concludes this article.

II. SYSTEM STRUCTURE AND ANALYSIS

A. System Structure

Fig. 1 shows the DWPT system, which consists of the EV side and ground side. The EV side composes of compensation

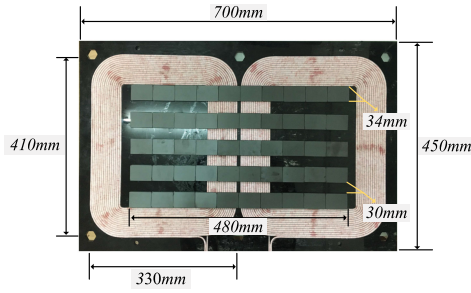


Fig. 2. Structure and dimensions of the magnetic coil.

topology, dc–dc converter, full-bridge rectifier, battery load, and the receiver coil installed on the EV chassis. The ground side composes compensation topology, full-bridge inverter, ac/dc converter and the transmitter coils embedded in the driving lane.

As illustrated in Fig. 1, K_1 , K_2 , and K_3 represent switches on the input dc bus and the current sensors are used to measure the current of each transmitter panel. When the system working with no-load, the primary current of the input dc bus would increase considerably. If the detected current is greater than the protection threshold, switches will turn OFF to cut off the input dc source. Then, reliability and safety issues can be guaranteed through this protection configuration.

Remark 1: Refer to Section II-C, a double-sided LCC compensation network is provided with current-source output characteristic. If the system works in no-load condition, i.e., the load resistor is infinity, the required power from the dc source is infinity theoretically, resulting in an infinity input current. Checking the protection threshold is a feasible and effective protection configuration to conquer these safety issues.

B. Magnetic Coil Analysis

A DD magnetic coil is designed to realize the DWPT system, as shown in Fig. 2. The length and width of the coil are 700 and 450 mm, respectively. The unipolar rectangular coil size is 410×330 mm, and the turns of the coil are 16. In order to improve the magnetic field, five ferrite core arrays are distributed uniformly on the DD coil. The size of each core array is 480×34 mm and the interval between adjacent arrays is 30 mm.

In the DWPT system, the interval between adjacent transmitter coils is 450 mm and the nominal transmission gap is 200 mm. The misalignment along the driving direction is denoted by Y-misalignment, and it increases when the receiver coil moves from the first transmitter coil to the next transmitter coil. The process, while Y-misalignment increases from 0 to 90 cm, represents an entire DWPT window.

Fig. 3 shows two sets of transmitter side with one set of receiver side in DWPT. L_1 , L_2 , and L_s denote the first transmitter coil, the secondary transmitter coil, and the receiver coil, respectively. In this topology, L_1 is coupled with L_s , L_2 is coupled with L_s , and L_1 is coupled with L_2 , and the corresponding mutual inductors are M_{1s} , M_{2s} , and M_{12} . The total mutual inductor is

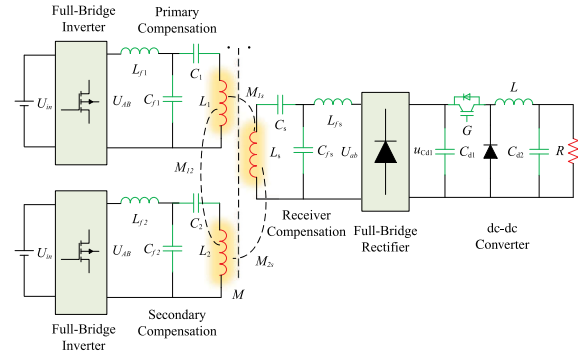


Fig. 3. Topology of DWPT system.

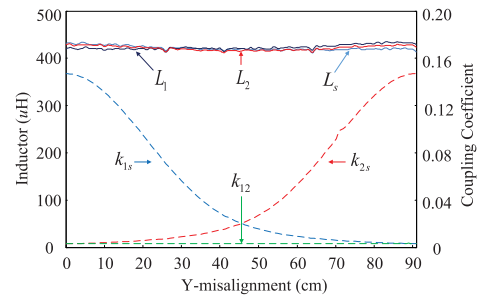


Fig. 4. Self-inductors and coupling coefficients during the DWPT window.

denoted by M , and these inductors can be described by

$$\begin{cases} M_{1s} = k_{1s} \cdot \sqrt{L_1 L_s} \\ M_{2s} = k_{2s} \cdot \sqrt{L_2 L_s} \\ M_{12} = k_{12} \cdot \sqrt{L_1 L_2} \\ M = M_{1s} + M_{2s} + M_{12} \end{cases} \quad (1)$$

where k_{1s} , k_{2s} , and k_{12} represent coupling coefficients.

As shown in Fig. 4, the variation of inductors and coupling coefficients during a DWPT window are analyzed by ANSYS Maxwell software. The simulation results show that L_1 , L_2 , and L_s remain around 420 μH and, thus, they can be considered constant. The k_{12} is about 0.004 and, thus, M_{12} can be neglected. It is easy to find that k_{1s} decreases and k_{2s} increases rapidly with the increasing Y-misalignment. Therefore, M varies quickly on a large scale and the effect of M_{12} can be negligible. Thereby, M in (1) becomes $M = M_{1s} + M_{2s}$.

C. Receiver-Side Transfer Power Regulation

Fig. 3 depicts the topology of DWPT system. In this system, U_{in} represents the input dc voltage, and R is the equivalent resistor of the dc load. L_{f1} , C_{f1} , and C_1 are the first compensation topology; L_{f2} , C_{f2} , and C_2 are the secondary compensation topology; and L_{fs} , C_{fs} , and C_s represent the receiver compensation topology. ω and f_s denote the operating angular frequency and the operating frequency, respectively. To form a

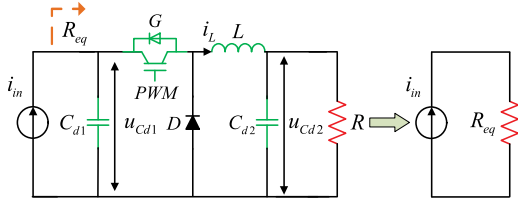


Fig. 5. dc-dc converter in DWPT system.

resonant tank [14], giving

$$\begin{cases} \omega L_1 - (\omega C_1)^{-1} - (\omega C_{f1})^{-1} = 0 \\ \omega L_{f1} - (\omega C_{f1})^{-1} = 0 \\ \omega L_2 - (\omega C_2)^{-1} - (\omega C_{f2})^{-1} = 0 \\ \omega L_{f2} - (\omega C_{f2})^{-1} = 0 \\ \omega L_s - (\omega C_s)^{-1} - (\omega C_{fs})^{-1} = 0 \\ \omega L_{fs} - (\omega C_{fs})^{-1} = 0 \end{cases}. \quad (2)$$

In resonant working condition, transfer power of double-sided LCC topology can be described as [14]

$$P_{\text{out}} = \frac{M}{\omega L_{f1} L_{fs}} U_{AB} U_{ab} \quad (3)$$

where U_{AB} denotes first-order rms value of output voltage of the full-bridge inverter and U_{ab} denotes first-order rms value of input voltage of the full-bridge rectifier. In a fixed DWPT system, the values of L_{f1} , L_{fs} , and ω are constant. And U_{AB} is determined by U_{in} , which is also constant in this article. Therefore, transfer power is proportional to M and U_{ab} . When the mutual inductor varies quickly in a large scale during the DWPT window, transfer power can be improved by controlling U_{ab} .

Remark 2: U_{ab} and u_{Cd1} are input and output voltage of the full-bridge rectifier, respectively. U_{ab} is proportional to u_{Cd1} , and it can be regulated by the dc-dc converter on the receiver side. In other words, it is a feasible and practical approach to regulate the transfer power by controlling u_{Cd1} .

From the output of the full-bridge rectifier, the equivalent circuit of the DWPT system on the receiver side is shown in Fig. 5. Due to the current-source output characteristic of double-sided LCC compensation network [14], [15], the input of dc-dc converter can be regarded as an ideal current source, and it is represented by i_{in} . For high efficiency and power density, the dc-dc converter is designed to operate in continuous conduction mode. According to Norton's theorem, the buck dc-dc converter can be equivalent to a current source series connected with an equivalent resistor. From Fig. 5, we get

$$R_{eq} = \frac{R}{d^2} \quad (4)$$

where $d \in [0, 1]$ and R_{eq} denote the duty cycle and the equivalent resistor of this converter, respectively. Then, the output power can be improved by the buck converter during the DWPT window.

Remark 3: The buck converter is adopted in this DWPT system, and the regulating range of R_{eq} is R to $+\infty$. Through the regulation of buck converter's duty cycle d , the equivalent

resistor and input voltage u_{Cd1} can be adjusted dynamically to regulate the output power.

III. PASSIVITY-BASED PI CONTROL

The topology of the buck dc-dc converter in DWPT system is shown in Fig. 5. The parasitic parameters are neglected and, thus, the differential equations describing the state average model are given by

$$\begin{cases} L \frac{di_L}{dt} = d \times u_{Cd1} - u_{Cd2} \\ C_{d1} \frac{du_{Cd1}}{dt} = i_{in} - d \times i_L \\ C_{d2} \frac{du_{Cd2}}{dt} = i_L - \frac{u_{Cd2}}{R} \end{cases} \quad (5)$$

where C_{d1} , C_{d2} , and L denote the input capacitor, output capacitor, and inductor, respectively. u_{Cd1} , u_{Cd2} , i_L , and i_{in} represent the input capacitor voltage, output capacitor voltage, the inductor current, and the input current, respectively.

A. Passivity-Based Control

The port-controlled hamiltonian (PCH) can be described as follows [34]:

$$\begin{cases} \dot{x} = [J(x) - R(x)] \cdot \frac{\partial H(x)}{\partial x} + \zeta + g(x)u \\ y = g^T(x) \frac{\partial H(x)}{\partial x} \end{cases} \quad (6)$$

where $x \in R^n$ is the state vector; $J, R: R^n \rightarrow R^{n \times n}$ are the interconnection and dissipation matrices, respectively, with $J(x) = -J^T(x)$ and $R(x) = R^T(x)$; $H: R^n \rightarrow R$ is the total stored energy function; $g: R^n \rightarrow R^{n \times m}$ is the input matrices; ζ represents the external force; and $u, y \in R^m$, $m < n$, are the control and output function, respectively.

From the energy view point, the energy of the dynamic system is stored in energy storage elements, such as inductor and capacitor. And the storage energy of inductor and capacitor can be calculated by $W_{Li} = \frac{1}{2} L_i i_{Li}^2$ and $W_{Ci} = \frac{1}{2} C_i u_{Ci}^2$, respectively, where i_{Li} and u_{Ci} denote current on L_i and voltage of C_i . The total energy function is given as

$$\begin{aligned} H(x) &= W_L + W_{Cd1} + W_{Cd2} \\ &= \frac{1}{2L} x_1^2 + \frac{1}{2C_{d1}} x_2^2 + \frac{1}{2C_{d2}} x_3^2 \end{aligned} \quad (7)$$

where $x = [x_1, x_2, x_3]^T = [L \cdot i_L, C_{d1} \cdot u_{Cd1}, C_{d2} \cdot u_{Cd2}]^T$, and x_1 , x_2 , and x_3 represent the inductor flux, the charge in the input capacitor, and the charge in the output capacitor, respectively.

Combing (5) with (6), the dynamic system (5) can be written in the form of PCH, which yields

$$\begin{aligned} J(x) &= \begin{pmatrix} 0 & 0 & -1 \\ 0 & 0 & 0 \\ 1 & 0 & 0 \end{pmatrix}, R(x) = \begin{pmatrix} 0 & 0 & 0 \\ 0 & 0 & 0 \\ 0 & 0 & \frac{1}{R} \end{pmatrix} \\ \zeta &= \begin{pmatrix} 0 \\ i_{in} \\ 0 \end{pmatrix}, g(x) = \begin{pmatrix} \frac{x_2}{C_{d1}} \\ -\frac{x_1}{L} \\ 0 \end{pmatrix}. \end{aligned}$$

Proof: Refer to (5), the average model becomes

$$\begin{cases} \dot{x}_1 = d \times \frac{x_2}{C_{d1}} - \frac{x_3}{C_{d2}} \\ \dot{x}_2 = i_{in} - d \times \frac{x_1}{L} \\ \dot{x}_3 = \frac{x_1}{L} - \frac{x_3}{C_{d2}R} \end{cases}. \quad (8)$$

The derivation of $H(x)$ with respect to x , we get

$$\frac{\partial H(x)}{\partial x} = \begin{pmatrix} \frac{x_1}{L} & 0 & 0 \\ 0 & \frac{x_2}{C_{d1}} & 0 \\ 0 & 0 & \frac{x_3}{C_{d2}} \end{pmatrix}. \quad (9)$$

Then, substituting (8) and (9) in (6), the dynamic system (5) takes the PCH form

$$\begin{aligned} \dot{x} = & \left(\begin{pmatrix} 0 & 0 & -1 \\ 0 & 0 & 0 \\ 1 & 0 & 0 \end{pmatrix} - \begin{pmatrix} 0 & 0 & 0 \\ 0 & 0 & 0 \\ 0 & 0 & \frac{1}{R} \end{pmatrix} \right) \\ & \times \begin{pmatrix} \frac{x_1}{L} & 0 & 0 \\ 0 & \frac{x_2}{C_{d1}} & 0 \\ 0 & 0 & \frac{x_3}{C_{d2}} \end{pmatrix} + \begin{pmatrix} 0 \\ i_{in} \\ 0 \end{pmatrix} + \begin{pmatrix} \frac{x_2}{C_{d1}} \\ -\frac{x_1}{L} \\ 0 \end{pmatrix} d. \end{aligned} \quad (10)$$

In this article, fix a desired equilibrium point x^* , the expected energy function can be written as

$$\begin{aligned} H_d(x) = & \frac{1}{2L}(x_1 - x_1^*)^2 + \frac{1}{2C_{d1}}(x_2 - x_2^*)^2 \\ & + \frac{1}{2C_{d2}}(x_3 - x_3^*)^2. \end{aligned} \quad (11)$$

Assume there are matrices $J_d(x) = -J_d^T(x)$, $R_d(x) = R_d^T(x) \geq 0$ and $H_d(x)$ is such that

$$x^* = \arg \min H_d(x). \quad (12)$$

Then, assume there exists $u = \beta(x)$, the closed-loop dynamic system (5) can be rewritten as follows:

$$\dot{x} = [J_d(x) - R_d(x)] \frac{\partial H_d(x)}{\partial x} \quad (13)$$

with x^* a stable equilibrium. According to La Salle's invariant principle, if the largest invariant set under the closed-loop dynamics (13) contained in

$$\left\{ x \in R^n \mid \frac{\partial H_d^T(x)}{\partial x} R_d \frac{\partial H_d(x)}{\partial x} = 0 \right\} \quad (14)$$

equals $\{x^*\}$. Then, the closed-loop system is asymptotically stable.

Substituting $u = \beta(x)$ into (6) yields (13). Since $J_d(x)$ is skew-symmetric matrix and $R_d(x)$ is positive-symmetric matrix, the time derivative of the storage function is obtained

$$\dot{H}_d(x) = - \left(\frac{\partial H_d(x)}{\partial x} \right)^T R_d \frac{\partial H_d(x)}{\partial x} \leq 0 \quad (15)$$

then, x^* is a stable equilibrium point and $H_d(x)$ can be regarded as a Lyapunov function. Based on La Salle's invariant principle and the conclusion (15), the dynamic system is proved to be asymptotically stable.

Combining (6) with (13), we have

$$\begin{aligned} & [J_d(x) - R_d(x)] \frac{\partial H_d(x)}{\partial x} \\ & = [J(x) - R(x)] \frac{\partial H(x)}{\partial x} + \zeta + g(x)u. \end{aligned} \quad (16)$$

Assume that $H_d(x) = H(x) + H_a(x)$, $J_d(x) = J(x) + J_a(x)$, $R_d(x) = R(x) + R_a(x)$, $u = d$, and $K(x) = \partial H_a(x)/\partial x = \partial H_d(x)/\partial x - \partial H(x)/\partial x$. In this article, we choose $J_d(x) = 0$, $R_d(x) = \text{diag}(r_1, 1/r_2, 1/r_3)$, where $r_1, r_2, r_3 > 0$ are the injected virtual impedances. Then, (16) can be rewritten as follows:

$$\begin{aligned} & [J_d(x) - R_d(x)] K(x) \\ & = -[J_a(x) - R_a(x)] \frac{\partial H(x)}{\partial x} + g(x)u + \zeta \end{aligned} \quad (17)$$

where

$$\begin{aligned} J_a(x) & = \begin{pmatrix} 0 & 0 & 1 \\ 0 & 0 & 0 \\ -1 & 0 & 0 \end{pmatrix} \\ R_a(x) & = \begin{pmatrix} r_1 & 0 & 0 \\ 0 & \frac{1}{r_2} & 0 \\ 0 & 0 & \frac{1}{r_3} - \frac{1}{R} \end{pmatrix}. \end{aligned}$$

Substituting $K(x) = [-x_1^*/L, -x_2^*/C_{d1}, -x_3^*/C_{d2}]^T$ into (17), we obtain

$$\begin{aligned} \begin{pmatrix} -r_1 & 0 & 0 \\ 0 & \frac{-1}{r_2} & 0 \\ 0 & 0 & \frac{-1}{r_3} \end{pmatrix} K(x) & = \begin{pmatrix} r_1 & 0 & -1 \\ 0 & \frac{1}{r_2} & 0 \\ 1 & 0 & \frac{1}{r_3} - \frac{1}{R} \end{pmatrix} \frac{\partial H(x)}{\partial x} \\ & + \begin{pmatrix} 0 \\ 1 \\ 0 \end{pmatrix} i_{in} + \begin{pmatrix} \frac{x_2}{C_{d1}} \\ -\frac{x_1}{L} \\ 0 \end{pmatrix} d. \end{aligned} \quad (18)$$

Now, (18) can be further simplified, that is,

$$\begin{cases} \frac{r_1 x_1^*}{L} = \frac{r_1 x_1}{L} - \frac{x_3}{C_{d2}} + \frac{x_2}{C_{d1}} \times d \\ \frac{x_2^*}{r_2 C_{d1}} = \frac{x_2}{r_2 C_{d1}} + i_{in} - d \times \frac{x_1}{L} \\ \frac{x_3^*}{r_3 C_{d2}} = \frac{x_1}{L} + \left(\frac{1}{r_3} - \frac{1}{R} \right) \frac{x_3}{C_{d2}} \end{cases}. \quad (19)$$

Here, substituting $x = [L \cdot i_L, C_{d1} \cdot u_{Cd1}, C_{d2} \cdot u_{Cd2}]^T$ into (19), i_L^* and u_{Cd1}^* represent the reference value of i_L and u_{Cd1} , respectively. Then, the duty ratio becomes

$$d = \frac{u_{Cd2} + r_1(i_L^* - i_L)}{u_{Cd1}} \quad (20)$$

$$d = \frac{i_{in}}{i_L} - \frac{u_{Cd1}^* - u_{Cd1}}{r_2 i_L} \quad (21)$$

where (20) and (21) are calculated from the first and secondary formula of (19), respectively.

Refer to Section II-C, (21) can be applied to regulate the transfer power by controlling u_{Cd1} . However, i_{in} , i.e., the output current of the full-bridge rectifier, is a high-frequency sinusoidal half-wave signal, which is not able to measure by the current sensor. In order to improve the PBC performance, we design a

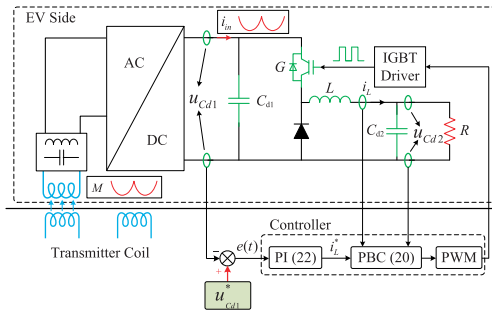


Fig. 6. Systematic control block diagram.

PI controller to operate with (20) for controlling u_{Cd1} , and the implementation is shown in Section III-B.

B. Complementary PI Controller

The frequency of i_{in} is determined by the resonant frequency. In this article, i_{in} is a 170 kHz sinusoidal half-wave signal. Meanwhile, the amplitude of i_{in} varies rapidly on a large scale along with the variable mutual inductor. Moreover, the changing speed depends on the driving speed towards the transmitter coils. To simplify the analysis, the influence of the Y-misalignment on the coupling coefficient only has been considered as shown in Fig. 2. At the same time, the X-misalignment (i.e., the misalignment of the vertical driving direction) is inevitable and random when the EV is in-motion. Therefore, it is tough to detect i_{in} by the current sensor.

In order to address these issues, a complementary PI controller is designed and combined with the PBC (20) and thus, a PIPBC scheme is proposed. Let $e(t) = u_{Cd1}^* - u_{Cd1}$ represent the steady-state error of u_{Cd1} , which is the input of PI regulator

$$i_L^* = K_p e(t) + K_i \int_0^t e(\tau) d\tau, \quad |i_L^*| \leq I_M \quad (22)$$

where $K_p, K_i > 0$. In order to protect the power electronic components, I_M is introduced to limit the maximum value of the desired current. The output of the PI controller (22) is the input of PBC (20), where i_L^* is the desired current of PBC. And the systematic control block diagram is shown in Fig. 6.

IV. SIMULATION RESULTS

Both simulation and experiments are implemented to verify the proposed PIPBC scheme and its effectiveness for the dynamic wireless charging system. The DWPT system specifications are listed in Table I, and Table II shows the circuit parameters for the compensation topology. This section shows the simulation results, and the experimental results are demonstrated in Section V.

A. Simulation Results of Resistor Load

To verify the dynamic performance and robustness against the variable load of the proposed controller, transient response tests, load variation tests, and dynamic charging tests have been carried out in the PLECS.

TABLE I
SPECIFICATIONS OF DWPT SYSTEM

Parameter	Design Value
Input dc-dc voltage U_{in}	260V
Reference input voltage in dynamic charging u_{Cd1}^*	180V
Operating frequency f_s	85 kHz
Input capacitor of the dc-dc converter C_{d1}	165 μ F
Output capacitor of the dc-dc converter C_{d2}	470 μ F
Inductor of the dc-dc converter L	1.38 mH
Switching frequency of the dc-dc converter f	20 kHz
Resistor load R	11 Ω
Battery load U_b	100 V
Maximum power	2.63 kW
Maximum efficiency	91.06 %

TABLE II
PARAMETERS FOR COMPENSATION TOPOLOGY

Parameter	Design Value	Measure Value
First transmitter coil inductor L_1	420 μ H	418 ~ 422 μ H
Secondary transmitter coil inductor L_2	420 μ H	418 ~ 422 μ H
Receiver coil inductor L_s	420 μ H	421 ~ 425 μ H
First transmitter resonant inductor L_{f1}	45 μ H	45.6 ~ 46.2 μ H
Secondary transmitter resonant inductor L_{f2}	45 μ H	45.2 ~ 45.8 μ H
Receiver resonant inductor L_{fs}	45 μ H	45.8 ~ 46.5 μ H
First transmitter resonant capacitor C_{f1}	78.47 nF	78.3 nF
Secondary transmitter resonant capacitor C_{f2}	78.47 nF	78.1 nF
Receiver resonant capacitor C_{fs}	78.47 nF	78.20 nF
First transmitter compensation capacitor C_1	9.64 nF	9.72 nF
Secondary transmitter compensation capacitor C_2	9.64 nF	9.77 nF
Receiver compensation capacitor C_s	9.64 nF	9.81 nF

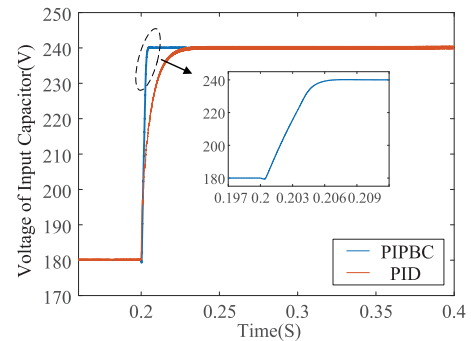


Fig. 7. Transient response performance of simulation results.

Case 1: Tests of Transient Response.

In order to validate the transient performance of the proposed PIPBC to regulate the transfer power, a comparison is made with the PID algorithm. In this transient response test, the Y-misalignment of the receiver coil is 0 cm. And reference value of the input voltage u_{Cd1} changes from 180 to 240 V suddenly at 0.2 s. Fig. 7 illustrates the simulation results of the transient response tests. And it shows that the transient time of the PIPBC and PID are 8 and 38 ms, respectively. Therefore, the superior transient performance of the proposed PIPBC is verified.

Because the mutual inductor M changes rapidly on a large scale during the DWPT window, good transient response is vital

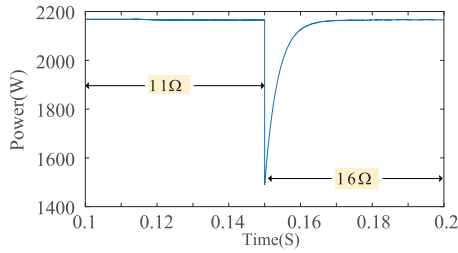


Fig. 8. Simulation results of load variation.

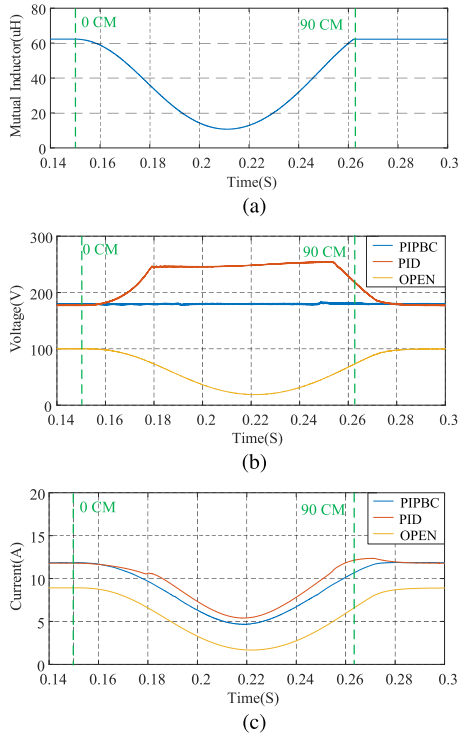


Fig. 9. Simulation results of the DWPT system for resistor load at low speed (35 km/h). (a) Mutual inductor. (b) The input voltage of the dc–dc converter. (c) The output current of the DWPT system.

for tracking the variable mutual inductor to adjust the system rapidly. Thus, it can ensure the reliability of the DWPT system.

Case 2: Test of Load Variation.

In the variable load test, the mutual inductor M is constant, and the output load changes from 11 to 16 Ω suddenly at 0.15 s. Fig. 8 demonstrates the simulation response curve for transfer power under variable load. It shows that the transfer power is around 2175 W when the load is 11 Ω , and output power can recover to 2175 W quickly when the load varies to 16 Ω . Therefore, the robustness against the variable load is verified.

Case 3: Dynamic Charging Tests.

To validate the dynamic performance of the proposed control algorithm, the dynamic wireless charging tests under OPEN, PID, and PIPBC schemes are carried out in PLECS at low and high speed. The OPEN scheme represents dynamic wireless charging without buck dc–dc converter (OPEN_WITHOUT_dc–dc). Figs. 9 and 10 show the simulation results marked with starting (0 CM) and ending (90 CM)

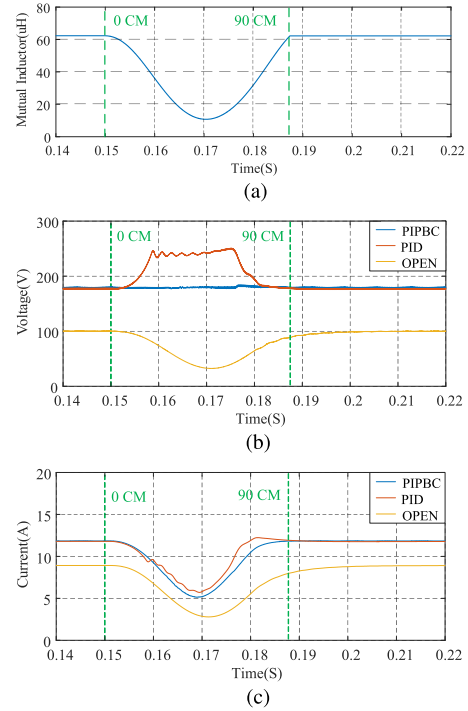


Fig. 10. Simulation results of the DWPT system for resistor load at high speed (120 km/h). (a) Mutual inductor. (b) The input voltage of the dc–dc converter. (c) The output current of the DWPT system.

position of the DWPT window, when the receiver coil is moving at low speed (35 km/h) and high speed (120 km/h), respectively. Compared with OPEN_WITHOUT_dc–dc, the reference value of the input voltage u_{Cd1}^* is 180 V in PID and PIPBC schemes. At $t = 0.15$ s, the receiver coil starts to move over the transmitter coils. Because the mutual inductor changes rapidly on a large scale during the DWPT window, three different performances are under the above three schemes.

In OPEN_WITHOUT_dc–dc, simulation results show that the output current and transfer power change along with the mutual inductor. Furthermore, the systematic power decreases to around zero when the receiver coil arrives in the middle of the adjacent transmitter coils. In the PID scheme, simulation results indicate that input voltage u_{Cd1} and the output current have been improved through closed-loop control, so as to improve the systematic power. However, it fails to follow the changing mutual inductor to adjust rapidly, which deteriorates the dynamic performance and the DWPT system's reliability, resulting in an apparent deviation between u_{Cd1} and the reference value. Moreover, the jitter of the output current and u_{Cd1} increase with the moving speed. Due to the superior transient response, in the PIPBC scheme, simulation results show that the DWPT under PIPBC scheme can track the variable mutual inductor to keep u_{Cd1} at the reference value. During the DWPT window, the output current has been improved to improve output power. Moreover, the proposed method has guaranteed the reliability of the DWPT system. Therefore, it validates the feasibility and remarkable performance of the DWPT-applied PIPBC.

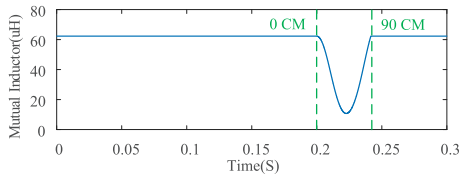


Fig. 11. Mutual inductor of the DWPT system for battery load.

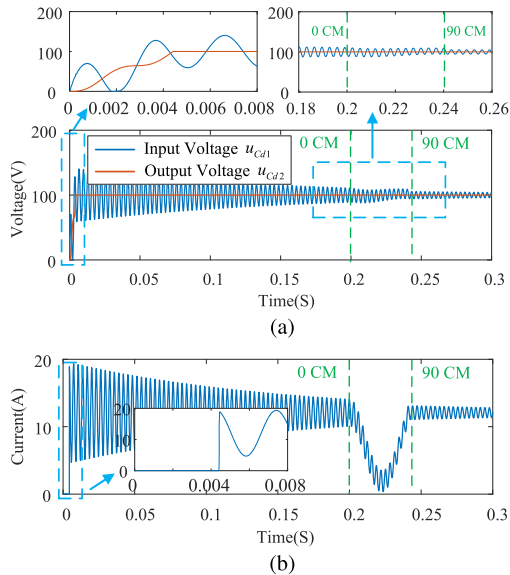


Fig. 12. Simulation results of the DWPT system for battery load in OPEN_WITHOUT_dc-dc scheme. (a) The input and output voltage of the dc-dc converter. (b) The output current of the DWPT system.

B. Simulation Results of Battery Load

In order to show good performance of this proposed controller for dynamic wireless charging system with battery load, simulation tests have been carried out in the PLECS. In these tests, the EV is driving at 35 km/h and the voltage of the battery load is 100 V. Similar to the tests with resistor load, the reference value of the input voltage u_{Cd1}^* is 180 V.

Fig. 11 shows the mutual inductor when the receiver coil is moving at 35 km/h. Figs. 12–14 demonstrate the simulation results for dynamic wireless charging system with battery load in OPEN_WITHOUT_dc-dc, PID, and PIPBC schemes, respectively. Besides, these results are marked with the starting and ending position of the DWPT window.

Different from the simulation tests with resistor load, the tests with battery load consist of start-up procedure and dynamic wireless charging procedure.

Case 1: Start-Up Procedure.

During the start-up procedure, the output voltage u_{Cd2} increases from zero and the output current is zero, while u_{Cd2} is less than 100. The simulation results suggest that the output current is zero until the output voltage is greater than or equal to the battery voltage. For convenience of representation, the start-up time is defined to represent the time while output current begins to grow from zero. Then, the start-up time in OPEN_WITHOUT_dc-dc, PID, and PIPBC schemes are 4.3, 5.1, and 2.9 ms, respectively. As depicted in Fig. 12(a), the

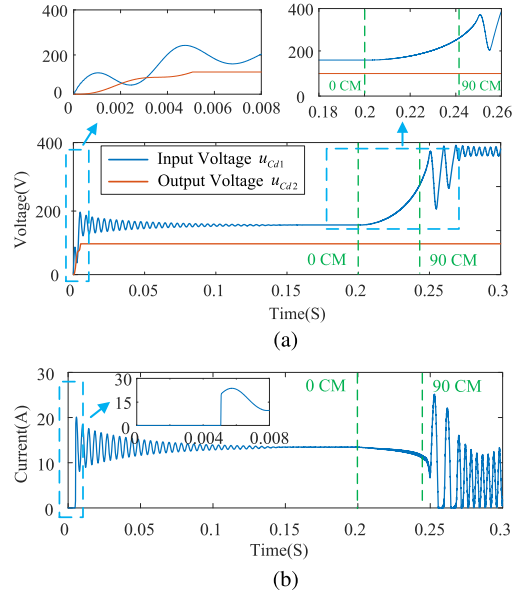


Fig. 13. Simulation results of the DWPT system for battery load in PID scheme. (a) The input and output voltage of the dc-dc converter. (b) The output current of the DWPT system.

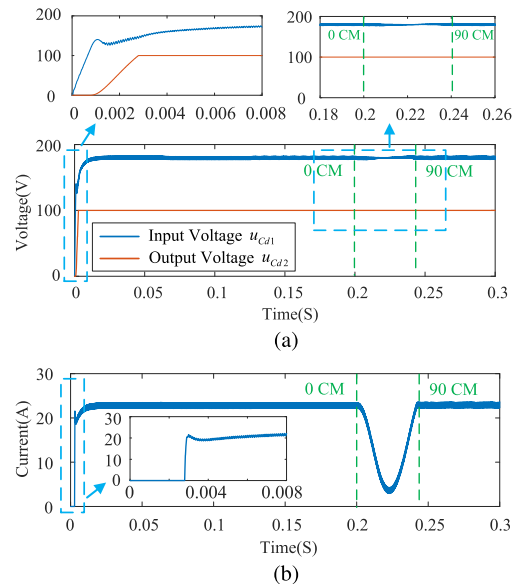
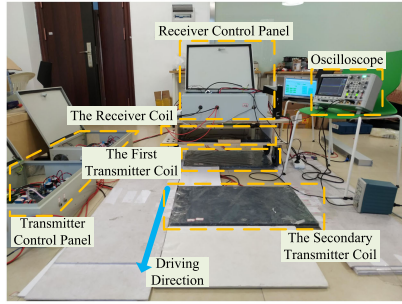


Fig. 14. Simulation results of the DWPT system for battery load in PIPBC scheme. (a) The input and output voltage of the dc-dc converter. (b) The output current of the DWPT system.

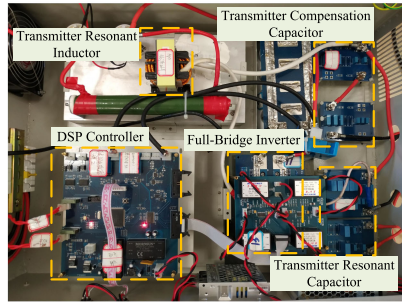
output current and output voltage u_{Cd2} are oscillatory under OPEN_WITHOUT_dc-dc. And Fig. 13(a) demonstrates that the oscillation would be addressed through PID in a long time. Therefore, the simulation results validate the good performance of the proposed controller.

Case 2: Dynamic Charging Procedure.

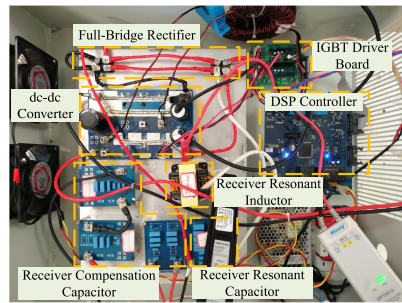
During the dynamic charging procedure, the input voltage u_{Cd1} oscillates around 100 V, i.e., the voltage of battery load, under OPEN_WITHOUT_dc-dc condition. The simulation results show that the output current changes along with the mutual inductor, and it also is oscillatory during the DWPT window.



(a)



(b)



(c)

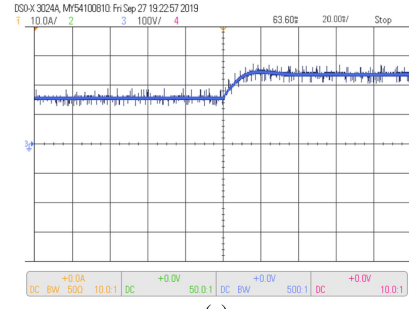
Fig. 15. Experimental setup. (a) Physical setup of DWPT system. (b) Experimental prototype of transmitter panel. (c) Experimental prototype of receiver panel.

Under PID scheme, simulation results show that input voltage u_{Cd1} fails to be adjusted according to the changing mutual inductor, resulting in oscillatory and instability. Moreover, it may lead to system impairments or even system failures.

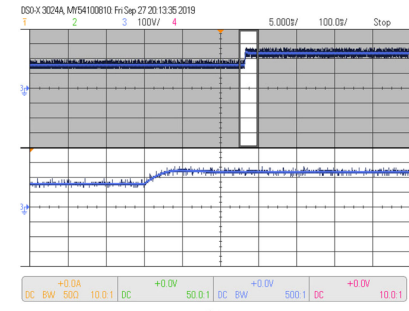
Similar to the tests with resistor load, simulation results show that the DWPT in PIPBC scheme can track the variable mutual inductor to keep u_{Cd1} at 180 V, i.e., the reference value. Due to a larger input voltage u_{Cd1} , it can also conclude that the output current has been improved to obtain a larger output power. Moreover, the reliability of the DWPT system has been improved by the proposed PIPBC. Therefore, it validates the feasibility and remarkable performance of the PIPBC-based DWPT with battery load.

V. EXPERIMENTAL RESULTS

To further validate the feasibility and effectiveness of the DWPT under PIPBC scheme, experimental results are supplied. Fig. 15 depicts the real hardware experimental setup. Fig. 15(a) shows the overall physical setup of the DWPT system; there are two transmitter panels and one receiver panel. Fig. 15(b)



(a)



(b)

Fig. 16. Transient response performance of experimental results. (a) PID. (b) PIPBC.

shows the experimental prototype of the transmitter panel, and Fig. 15(c) shows the experimental prototype of the receiver panel. The digital signal processing (DSP) controller in transmitter and receiver panels is TMS320F28335. A 2.2-kW DWPT system is built, and experiments with both resistor load and battery load are implemented as follows.

A. Experimental Results of Resistor Load

Case 1: Experiment of Transient Response.

Similar to the simulation tests, the mutual inductor M is constant, and the reference value of the input voltage u_{Cd1}^* changes from 180 to 240 V suddenly. Fig. 16 demonstrates the experimental results of transient response. It shows that the transient time of the PIPBC and PID are 6 and 35 ms, respectively. The results provide further validation of superior dynamic characteristics of PIPBC, and it agrees with the previous simulation conclusions.

Case 2: Experiment of Dynamic Charging.

Fig. 17 shows the experimental results marked with Y-misalignment during the DWPT window under three different schemes, and the mutual inductor versus Y-misalignment is measured and depicted in Fig. 17(a).

In OPEN_WITHOUT_dc-dc, the output current and output power change along with the mutual inductor. Moreover, systematic power decreases to around zero when Y-misalignment is 45 cm. In PID scheme, although the output current and output power have been improved through closed-loop control, failing to track the variable mutual inductor leads to an apparent deviation between u_{Cd1} and the reference value. The experimental results demonstrate that the stability of DWPT is no longer guaranteed. In the PIPBC scheme, Fig. 17(d) shows that the DWPT under PIPBC scheme can track the variable mutual

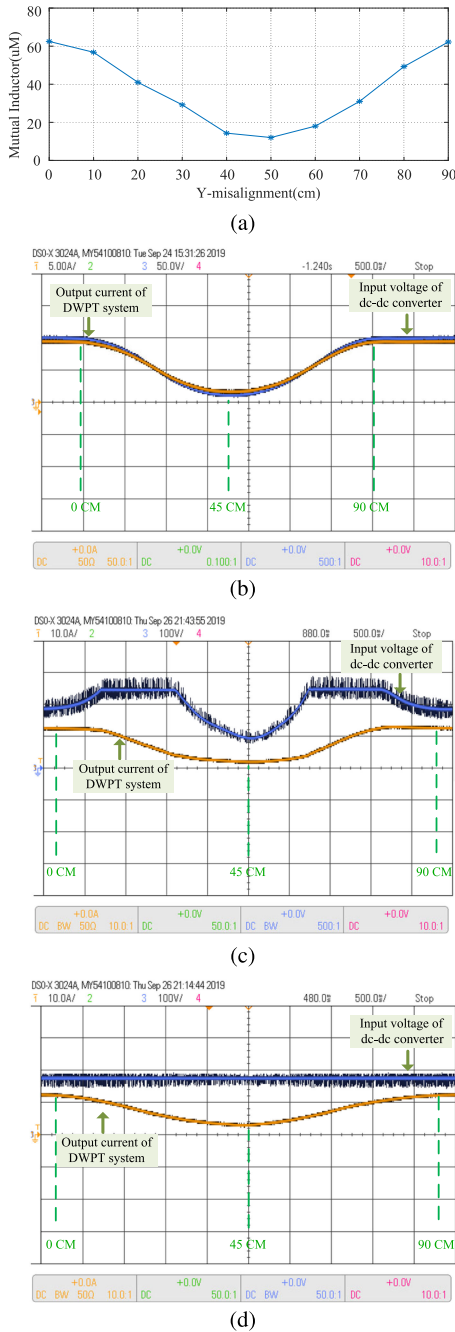


Fig. 17. Experimental results of the DWPT system with different control strategies. (a) Mutual inductor. (b) OPEN. (c) PID. (d) PIPBC.

inductor to regulate u_{Cd1} at the reference value. The output power has been improved, and the reliability of DWPT system has been guaranteed. The experimental results match with the previous simulation results. It can be concluded that the DWPT under the PIPBC scheme is reliable.

Case 3: Transfer Power and Efficiency.

A comparison between OPEN_WITHOUT_dc-dc and PIPBC scheme has been made in this case. Moreover, the transfer power and efficiency are measured during the DWPT window, as depicted in Fig. 18. It indicates that the output transfer power and efficiency under the PIPBC scheme are larger than those of

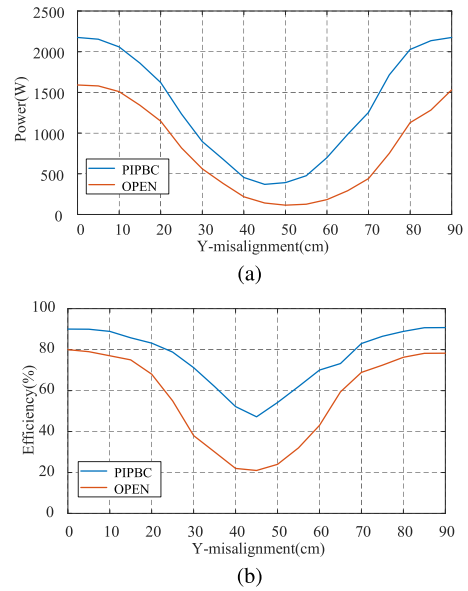


Fig. 18. Transfer power and efficiency during the DWPT window with resistor load. (a) Transfer power. (b) Transfer efficiency.

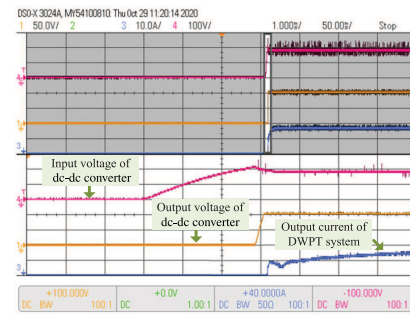


Fig. 19. Experimental results for start-up procedure of the DWPT system with battery load and the waveforms of input voltage u_{Cd1} , output voltage u_{Cd2} , and output current.

OPEN_WITHOUT_dc-dc. In OPEN_WITHOUT_dc-dc, the maximum transfer power is 1620 W, and the corresponding efficiency is 80.23%. In the PIPBC scheme, the maximum transfer power is 2175 W, and the corresponding efficiency is 90.12%.

B. Experimental Results of Battery Load

Similar to the simulation results, the experimental tests with battery load would be divided into start-up procedure and dynamic charging procedure.

Case 1: Start-Up Procedure.

Fig. 19 shows the experimental results of input voltage u_{Cd1} , output voltage u_{Cd2} , and output current under PIPBC scheme during the start-up procedure. Similarly, the output current is zero until the output voltage u_{Cd2} increases to be greater than or equal to the battery voltage. The experimental results demonstrate that the start-up time is 3.2 ms, and it matches well with the previous simulation results.

Case 2: Dynamic Charging Procedure.

During the dynamic charging procedure, the mutual inductor versus Y-misalignment is the same as that depicted in Fig. 17(a).

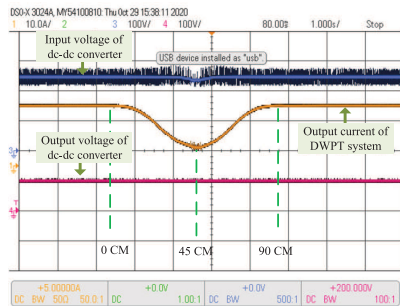


Fig. 20. Experimental results for dynamic charging procedure of the DWPT system with battery load and the waveforms of input voltage u_{Cd1} , output voltage u_{Cd2} , and output current.

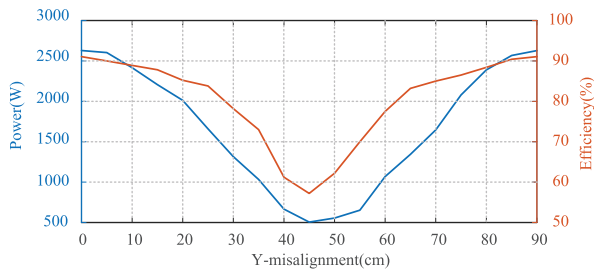


Fig. 21. Transfer power and efficiency during the DWPT window with battery load.

The experimental results under PIPBC scheme is shown in Fig. 20, and it demonstrates the experimental waveforms of input voltage u_{Cd1} , output voltage u_{Cd2} , and output current. The experimental results show that the DWPT under PIPBC scheme can track the variable mutual inductor to regulate u_{Cd1} at the reference value. Then, the feasibility and remarkable performance of the proposed PIPBC have been validated. It can be concluded that the PIPBC-based DWPT is reliable both with resistor and battery load.

Case 3: Transfer Power and Efficiency.

During the dynamic charging procedure with battery load, the systematic transfer power and efficiency are depicted in Fig. 21. Refer to the conclusion of PIPBC-based DWPT with resistor load, and it suggests that a larger systematic efficiency would be obtained with a larger output transfer power. As depicted in Figs. 18(a) and 21, the transfer power of DWPT with battery load is larger than that of the system with a resistor. It indicates that the output transfer power and efficiency are larger under the PIPBC scheme. The maximum transfer power is 2630 W, and the corresponding efficiency is 91.06%.

VI. CONCLUSION

In this article, the dynamic wireless charging system for EVs was considered. As the coupling coefficient between the transmitter coils and receiver coil varies rapidly on a large scale during the EVs moving, a dc-dc converter was added to cascade on the receiver side, and PIPBC was developed for the receiver-side control. Some simulation and experimental results were given to demonstrate the effectiveness of the DWPT with the PIPBC

scheme and its excellent performance in power transfer. It is also showed that, under the proposed design, the transfer efficiency can also be greater than that of OPEN_WITHOUT_dc-dc scheme.

Our future work is to install the designed wireless charging system on an EV, and it would focus on two aspects: 1) integrate transmitter and receiver coils with corresponding resonant inductor together to save space, and 2) develop a foreign object detection system according to the magnetic field.

REFERENCES

- [1] P. Si, A. P. Hu, S. Malpas, and D. Budgett, "A frequency control method for regulating wireless power to implantable devices," *IEEE Trans. Biomed. Circuits Syst.*, vol. 2, no. 1, pp. 22–29, Mar. 2008.
- [2] R. Tavakoli and Z. Pantic, "Analysis, design, and demonstration of a 25-kW dynamic wireless charging system for roadway electric vehicles," *IEEE J. Emerg. Sel. Topics Power Electron.*, vol. 6, no. 3, pp. 1378–1393, Sep. 2018.
- [3] B. J. Limb *et al.*, "Economic viability and environmental impact of in-motion wireless power transfer," *IEEE Trans. Transp. Electrification*, vol. 5, no. 1, pp. 135–146, Mar. 2018.
- [4] D. Patil *et al.*, "Wireless power transfer for vehicular applications: Overview and challenges," *IEEE Trans. Transp. Electr.*, vol. 4, no. 1, pp. 3–37, Dec. 2017.
- [5] C. Xiao, D. Cheng, and K. Wei, "An LCC-C compensated wireless charging system for implantable cardiac pacemakers: Theory, experiment, and safety evaluation," *IEEE Trans. Power Electron.*, vol. 33, no. 6, pp. 4894–4905, Jun. 2018.
- [6] M. Hutin and M. Leblanc, "Transformer system for electric railways," Patent US 527857, 1894.
- [7] Z. Zhang, H. Pang, A. Georgiadis, and C. Cecati, "Wireless power transfer – An overview," *IEEE Trans. Ind. Electron.*, vol. 66, no. 2, pp. 1044–1058, Feb. 2019.
- [8] S. Chopra and P. Bauer, "Driving range extension of EV with on-road contactless power transfer - A case study," *IEEE Trans. Ind. Electron.*, vol. 60, no. 1, pp. 329–338, Jan. 2013.
- [9] A. Kurs, A. Karalis, R. Moffatt, J. D. Joannopoulos, P. Fisher, and M. Soljacic, "Wireless power transfer via strongly coupled magnetic resonances," *Science*, vol. 317, no. 5834, pp. 83–86, Jul. 2007.
- [10] S. Choi, J. Huh, W. Y. Lee, S. W. Lee, and C. T. Rim, "New crosssegmented power supply rails for roadway-powered electric vehicles," *IEEE Trans. Power Electron.*, vol. 28, no. 12, pp. 5832–5841, Dec. 2013.
- [11] J. Kim, D. H. Kim, and Y. J. Park, "Analysis of capacitive impedance matching networks for simultaneous wireless power transfer to multiple devices," *IEEE Trans. Power Electron.*, vol. 62, no. 5, pp. 2807–2813, May 2015.
- [12] S. Zhou and C. C. Mi, "Multi-paralleled LCC reactive power compensation networks and their tuning method for electric vehicle dynamic wireless charging," *IEEE Trans. Ind. Electron.*, vol. 63, no. 10, pp. 6546–6556, Oct. 2016.
- [13] H. Feng, T. Cai, S. Duan, J. Zhao, X. Zhang, and C. Chen, "An LCC-compensated resonant converter optimized for robust reaction to large coupling variation in dynamic wireless power transfer," *IEEE Trans. Ind. Electron.*, vol. 63, no. 10, pp. 6591–6601, Oct. 2016.
- [14] S. Li *et al.*, "A double-sided LCC compensation network and its tuning method for wireless power transfer," *IEEE Trans. Veh. Technol.*, vol. 64, no. 6, pp. 2261–2273, Jun. 2015.
- [15] W. Li *et al.*, "Comparison study on SS and double-sided LCC compensation topologies for EV/PHEV wireless chargers," *IEEE Trans. Veh. Technol.*, vol. 65, no. 6, pp. 4429–4439, May 2015.
- [16] T. Diekhans and R. W. De Doncker, "A dual-side controlled inductive power transfer system optimized for large coupling factor variations and partial load," *IEEE Trans. Power Electron.*, vol. 30, no. 11, pp. 6320–6328, Jan. 2015.
- [17] M. Budhia, G. A. Covic, and J. T. Boys, "Design and optimization of circular structures for lumped inductive power transfer system," *IEEE Trans. Power Electron.*, vol. 26, no. 11, pp. 3096–3108, Nov. 2011.
- [18] H. Zeng *et al.*, "Optimization of magnetic core structure for wireless charging coupler," *IEEE Trans. Magn.*, vol. 53, no. 6, pp. 1–4, Jan. 2017.

- [19] M. Budhia, J. T. Boys, G. A. Covic, and C. Huang, "Development of a single-sided flux magnetic coupler for electric vehicle IPT charging systems," *IEEE Trans. Ind. Electron.*, vol. 60, no. 1, pp. 318–328, Jan. 2013.
- [20] H. Li, Y. Liu, K. Zhou, Z. He, W. Li, and R. Mai, "Uniform power IPT system with three-phase transmitter and bipolar receiver for dynamic charging," *IEEE Trans. Power Electron.*, vol. 34, no. 3, pp. 2013–2017, Mar. 2019.
- [21] Y. Liu, R. Mai, D. Liu, Y. Li, and Z. He, "Efficiency optimization for wireless dynamic charging system with overlapped DD coil arrays," *IEEE Trans. Power Electron.*, vol. 33, no. 4, pp. 2832–2846, Apr. 2018.
- [22] J. M. Miller, O. C. Onar, and M. Chinthavali, "Primary-side power flow control of wireless power transfer for electric vehicle charging," *IEEE J. Emerg. Sel. Topics Power Electron.*, vol. 3, no. 1, pp. 147–162, Mar. 2015.
- [23] C. Wang *et al.*, "Primary-side control method in two-transmitter inductive wireless power transfer systems for dynamic wireless charging applications," in *Proc. IEEE PELS Workshop Emer. Technol.: Wirel. Power*, 2017, pp. 1–6.
- [24] M. Fu, H. Yin, X. Zhu, and C. Ma, "Analysis and tracking of optimal load in wireless power transfer systems," *IEEE Trans. Power Electron.*, vol. 30, no. 7, pp. 3952–3963, Jul. 2015.
- [25] D. Kobayashi, T. Imura, and Y. Hori, "Real-time coupling coefficient estimation and maximum efficiency control on dynamic wireless power transfer for electric vehicles," in *Proc. IEEE PELS Workshop Emer. Technol.: Wirel. Power*, Daejeon, 2015, pp. 1–6.
- [26] L. Guo, J. Y. Hung, and R. M. Nelms, "Evaluation of DSP-based PID and fuzzy controllers for DC–DC converters," *IEEE Trans. Ind. Electron.*, vol. 56, no. 6, pp. 2237–2248, Jun. 2009.
- [27] T. K. Nizami and C. Mahanta, "An intelligent adaptive control of DC–DC buck converters," *IEEE Trans. Ind. Electron.*, vol. 353, no. 12, pp. 2588–2613, Aug. 2016.
- [28] S. Ding, W. X. Zheng, J. Sun, and J. Wang, "Second-order sliding-mode controller design and its implementation for buck converters," *IEEE Trans. Ind. Informat.*, vol. 14, no. 5, pp. 1990–2000, May 2018.
- [29] R. Ortega, A. Loria, P. J. Nicklasson, and H. Sira-Ramirez, "Passivity-Based Control of Euler-Lagrange Systems: Mechanical, Electrical and Electromechanical Applications," Berlin, Germany: Springer Science & Business Media, 1998.
- [30] M. Perez, R. Ortega, and J. R. Espinoza, "Passivity-based PI control of switched power converters," *IEEE Trans. Control Syst. Technol.*, vol. 12, no. 6, pp. 881–890, Nov. 2004.
- [31] T. S. Lee, "Lagrangian modeling and passivity-based control of three-phase AC/DC voltage-source converters," *IEEE Trans. Ind. Electron.*, vol. 51, no. 4, pp. 892–902, Aug. 2004.
- [32] J. Wang, X. Mu, and Q. K. Li, "Study of passivity-based decoupling control of T-NPC PV grid-connected inverter," *IEEE Trans. Ind. Electron.*, vol. 64, no. 9, pp. 7542–7551, Mar. 2017.
- [33] M. M. Namazi, S. M. S. Nejad, A. Tabesh, A. Rashidi, and M. Liserre, "Passivity-based control of switched reluctance-based wind system supplying constant power load," *IEEE Trans. Ind. Electron.*, vol. 65, no. 12, pp. 9550–9560, Mar. 2018.
- [34] M. Cupelli *et al.*, "Port controlled hamiltonian modeling and IDA-PBC control of dual active bridge converters for DC microgrids," *IEEE Trans. Ind. Electron.*, vol. 66, no. 11, pp. 9065–9075, Mar. 2019.
- [35] A. Jaafar, A. Alawieh, R. Ortega, E. Godoy, and P. Lefranc, "PI stabilization of power converters with partial state measurements," *IEEE Trans. Control Syst. Technol.*, vol. 21, no. 2, pp. 560–568, Feb. 2012.
- [36] M. Zhang *et al.*, "PID passivity-based control of port-hamiltonian systems," *IEEE Trans. Automat. Control*, vol. 63, no. 4, pp. 1032–1044, Jul. 2017.



Jia Liu received the B.S. degree in electrical engineering and its automation from the Hubei University of Technology, Wuhan, China, in 2015, and the M.S. degree in control science and engineering from the Wuhan University of Technology, Wuhan, in 2019. He is currently working toward the Ph.D. degree at the State Key Laboratory of Industrial Control Technology, Institute of Cyber-Systems and Control, Zhejiang University, Hangzhou, China.

His research interests include microgrids, passivity-based control, and wireless power transfer.



Zhitao Liu (Member, IEEE) received the B.S. degree from Shandong University at Weihai, China, in 2005, and the Ph.D. degree in control science and engineering from Zhejiang University, Hangzhou, China, in 2010.

From 2011 to 2014, he was a Research Fellow with TUM CREATE, Singapore. From 2015 to 2016, he was an Assistant Professor with the Institute of Cyber-Systems and Control, Zhejiang University, where he has been an Associate Professor since 2017. His current research interests include robust adaptive control, wireless transfer systems, and energy management systems.



Hongye Su (Senior Member, IEEE) was born in 1969. He received the B.S. degree in industrial automation from the Nanjing University of Chemical Technology, Jiangsu, China, in 1990, and the M.S. and Ph.D. degrees in industrial automation from Zhejiang University, Hangzhou, China, in 1993 and 1995, respectively.

From 1995 to 1997, he was a Lecturer with the Department of Chemical Engineering, Zhejiang University. From 1998 to 2000, he was an Associate Professor with the Institute of Advanced Process Control, Zhejiang University, where he is currently a Professor with the Institute of Cyber-Systems and Control. His research interests include robust control, time-delay systems, and advanced process control theory and applications.